modelling

MDPI

Article

Modeling the Stress Field in MSLA-Fabricated Photosensitive Resin Components: A Combined Experimental and Numerical Approach

Geraldo Cesar Rosario de Oliveira [1,2,*], Vania Aparecida Rosario de Oliveira [1,*], Carlos Alexis Alvarado Silva [2], Erick Siqueira Guidi [1] and Fernando de Azevedo Silva [1]

[1] Faculdade de Engenharia e Ciências, Câmpus de Guaratinguetá, Av, Universidade Estadual Paulista "Júlio de Mesquita Filho", Ariberto Pereira da Cunha, 333—Portal das Colinas—Guaratinguetá, São Paulo 12516-410, Brazil; erick.s.guidi@unesp.br (E.S.G.); fernando.azevedo@unesp.br (F.d.A.S.)
[2] Research Group Digital Manufacturing and Educational Innovation, Universidad Cesar Vallejo, Trujillo 13001, Peru; calvarados@ucv.edu.pe
* Correspondence: geraldo.arquivos@gmail.com (G.C.R.d.O.); vania.rosario@unesp.br (V.A.R.d.O.)

Abstract: This study presents an experimental and numerical investigation into the stress field in cylinders manufactured from photosensitive resin using the Masked Stereolithography (MSLA) technique. For material characterization, tensile and bending test data from resin specimens were utilized. The stress field in resin disks was experimentally analyzed using photoelasticity and Digital Image Correlation (DIC) methods, subjected to compressive loads, according to the cylinder–plane contact model. Images were captured during the experiments using polarizing film and a low-cost CPL lens, coupled to a smartphone. The experimental results were compared with numerical and analytical simulations, where the formation of fringes and regions indicating the direction and magnitude of normal and shear stresses were observed, with variations ranging from 0.6% to 8.2%. The convergence of the results demonstrates the feasibility of using parts produced with commercially available photosensitive resin on non-professional printers for studying contact theory and stress fields. In the future, this methodology is intended to be applied to studies on stress in gears.

Keywords: finite element; strain; DIC; photoelasticity; MSLA; low-cost mechanical tests

Academic Editor: Wei Gao

Received: 26 November 2024
Revised: 24 December 2024
Accepted: 6 January 2025
Published: 13 January 2025

Citation: Oliveira, G.C.R.d.; Rosario de Oliveira, V.A.; Alvarado Silva, C.A.; Guidi, E.S.; Silva, F.d.A. Modeling the Stress Field in MSLA-Fabricated Photosensitive Resin Components: A Combined Experimental and Numerical Approach. *Modelling* **2025**, *6*, 3. https://doi.org/10.3390/modelling6010003

1. Introduction

Understanding the stress and strain fields that arise due to contact under an external load is essential for the improvement and development of parts and components. Experimental analysis and simulation play a fundamental role in engineering, particularly in validating theoretical models and developing practical solutions using digital tools and additive manufacturing [1–3]. The synergy between material modeling and cutting-edge experimentation underpins modern engineering. The development of accurate constitutive models for polymeric materials is a priority in materials engineering, as it allows for predictions of how materials behave under different loading conditions and environments. In this context, various studies highlight theoretical and practical approaches that integrate advanced concepts of material mechanics. By implementing a constitutive model for amorphous polymers numerically, Bernard et al. [4] innovated by integrating it into finite element software (Abaqus), enabling its practical application in various industrial scenarios. The model was validated through compression tests and simulations of impact and flat forging deformation processes, demonstrating its effectiveness in predicting material behavior under extreme conditions. The development of three-dimensional constitutive models describing the nonlinear viscoelastic behavior of composite materials was advanced

by Varna and Pupure [5], who considered changes in material state, such as physical aging and variations in the degree of cure. Two models of different levels of complexity and precision were developed and demonstrated their applicability in numerical analyses of multiaxial loading, showing how three-dimensional conditions differ significantly from one-dimensional ones in terms of stresses and strains, highlighting the importance of 3D models for a more accurate representation of material behavior. The behavior of polymers and composites under large deformations was described by Abu Al-Rub et al. [6], who developed a comprehensive constitutive model integrating viscoelasticity, viscoplasticity, and viscodamage. The model was validated with experimental data obtained under various loading conditions, such as creep tests and constant strain rate tests, demonstrating its ability to capture the intricate behavior of these materials. The simulation of fractures in viscoelastic polymers using the phase-field method was modeled by Yin and Kaliske [7], combining viscoelasticity with strain-rate-dependent fracture mechanisms, and validating it in elastomers. Representative numerical studies were conducted to demonstrate the model's capability in more general applications, with results showing good agreement between simulations and experiments. The choice of mathematical model can significantly influence the description of polymeric materials, according to Kamenskikh [8]. The categorization of models into three main groups (elastic, elasto-plastic, and viscoelastic) revealed that accurate material behavior description is essential for computational engineering research. Such descriptions allow for qualitative predictions of a structure's performance throughout its lifecycle. Additionally, the study analyzes the impacts of this choice on contact and deformation problems, establishing a critical link between theoretical description and practical application.

Photoelasticity is a technique that leverages the double-refraction phenomenon in transparent materials under internal stress. The application of a load induces material deformations, generating stress fields that alter its optical properties. When illuminated with polarized light, interference patterns are produced, providing quantitative insights into the magnitude and distribution of internal stresses [9]. The photoelasticity technique remains a powerful tool for visualizing internal stresses in materials. Recent advancements include the integration of photosensitive resins and 3D printing, enabling new possibilities for analysis. The mechanical and photoelastic properties of transparent and photosensitive polymeric materials used in 3D printing, according to Wang et al. [10], depend on the chemical composition of these materials as well as methods to enhance their mechanical properties, such as print orientation, post-processing, and temperature control. Additionally, they tested the optical stress sensitivity of these materials, including visualization characteristics and performance under frozen stress conditions. Curtis et al. [11] investigated the use of stereolithography for fabricating three-dimensional models for photoelastic analysis. While the technique allows for rapid creation of complex components, challenges such as residual birefringence were identified in the process. To address these challenges, methodologies were proposed to minimize such effects, and comparisons were made between the properties of the resins used. In this field, the comprehensive review of advancements in digital photoelasticity over the last three decades by Ramesh and Sasikumar [12] stands out. They highlighted how this technique has evolved to solve complex engineering problems, emphasizing recent applications in areas such as biomedicine, civil engineering, and mechanical engineering, while encouraging the exploration of new challenges using this technique. The optical anisotropy of 3D-printed materials and its application in photoelasticity were described by Ren and Ju [13], who observed how the layers formed during printing affect light propagation and the optical behavior of the materials. Their findings contribute to a deeper understanding of the interaction between

microstructure and optical properties. These results are valuable for optimizing materials for more precise analyses.

Measurement techniques that utilize digital image correlation (DIC) have become a non-invasive and accessible method for measuring strains and stresses in materials. Recent studies highlight its potential in various applications, ranging from the validation of constitutive models to structural monitoring. In this research area, Arabul and Lunt [14] developed a low-cost device for measuring residual stresses using DIC combined with drilling. This innovative method significantly reduced the cost and time required for measurements, making the technique accessible for research laboratories and industrial applications. Practical examples of its use can be illustrated by Ghani et al. [15] and Kumar et al. [16], who demonstrated the application of the open-source software Ncorr for strain analyses in composites and masonry. They emphasized the technique's accuracy and versatility, showing that DIC is a viable alternative to traditional measurement methods. In testing, Quanjin et al. [17] applied DIC in tensile tests on materials such as aluminum, glass-fiber-reinforced plastics, and epoxy resin. The results confirmed the technique's effectiveness in capturing detailed strain data, reinforcing its use in complex mechanical characterizations. Maedeh et al. [18] investigated the transverse deformation of 3D-printed polymeric FG plates using numerical simulations and experimental measurements with 3D DIC. Results show good agreement between methods, despite larger discrepancies in nonlinear plates. The technique allows for optimizing material distribution to design plates with controlled stiffness and specific characteristics. The pursuit of quality and cost reduction in experimental procedures, according to [19–21], necessitates the use of open-source tools like Ncorr for Digital Image Correlation [22–24]. This method offers a viable alternative at significantly lower costs than traditional systems, which can be prohibitively expensive. In addition to DIC, photoelasticity [25,26] is an experimental technique that allows for real-time observation of stress fields in specimens [27–31]. While technologically advanced and precise methods exist for such analysis, this study prioritized low-cost solutions, developing a procedure using affordable polarizing filters and lenses integrated into portable devices.

The primary objective of this study was to investigate the behavior of the contact stress field in disks produced via additive manufacturing with photosensitive resin. The secondary objective was to develop a constitutive model of the material's behavior under loading for characterization in simulation software, with the potential for future application to more complex geometries.

The stress and strain field behavior was analyzed using the Finite Element Method and experimentally (with DIC and photoelasticity) on photosensitive resin disks manufactured via additive manufacturing using the MSLA method. The photosensitive resin was characterized through tensile and flexural tests. Compression of the disks was performed and recorded using a Shimadzu universal testing machine. The resin's constitutive model was developed in Ansys software (ansys 2024 r1) using force–displacement curves, elastic modulus, and Poisson's ratio obtained from the tests.

This study innovates by demonstrating the feasibility of complex stress field analyses using accessible resources, such as CPL lenses attached to smartphones and polarizing films, for experimental methods like photoelasticity and Digital Image Correlation (DIC). Additionally, it stands out for applying parts manufactured with photosensitive resins on non-professional printers to investigate contact theory and stress fields, promoting the use of cost-effective technologies in research contexts. The integration of experimental, numerical, and analytical methods validates the results, showcasing the effectiveness of these approaches. Finally, the proposal to apply this methodology to studies on stress in gears expands its practical applicability, consolidating its contribution to democratizing analysis techniques and fostering scientific and educational advancements with limited resources.

2. Materials and Methods

2.1. Manufacturing of the Parts

In this study, the specimens, gears, and disks were produced using the Saturn 2 Elegoo printer, as shown in Figure 1:

Figure 1. Printer used to produce the parts studied.

The printing parameters were as follows:

- Exposure time: 2.2 s
- Base exposure time: 20 s, with 5 base layers
- Layer height: 0.05 mm

The resin used was Anycubic Water-Wash Resin+, with characteristics provided by the manufacturer listed in Table 1.

Table 1. Characteristics of the resin used.

Characteristic	Units
UV Wavelength	365–405 nm
Density	1.15–1.20 g/cm^3
Hardness	80 Shore D
Tensile Strength	30–45 MPa
Elongation at Break	8–15%
Modulus of Elasticity	1600–1800 MPa
Flexural Strength	50–60 MPa
Flexural Modulus	1500–1600 MPa
Izod Impact Strength	50–60 J/m

After manufacturing, the parts underwent washing and curing. An Anycubic Wash&Cure Machine 3.0 was used for this process, as illustrated in Figure 2. Washing removes excess liquid resin from the surface of the parts. This process is essential to prevent unwanted solidification of resin residue that dripped during the removal of parts from the print bed, which could potentially alter the intended geometry of the parts. For the curing process, the parts were exposed to ultraviolet light for 60 min.

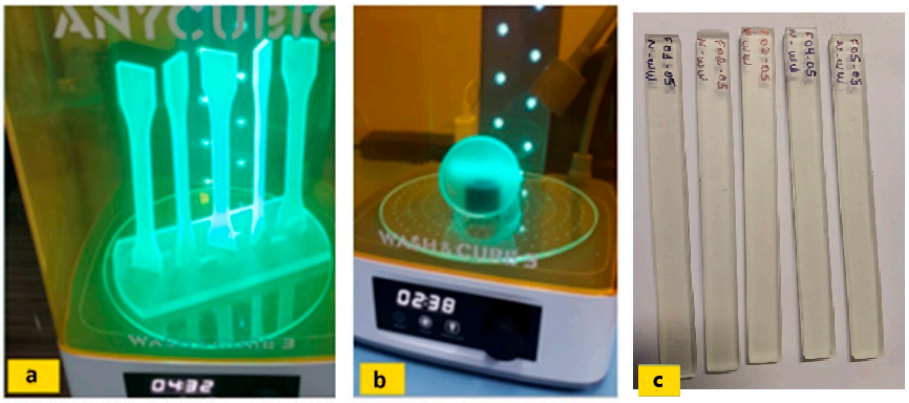

Figure 2. Wash and cure machine, parts exposed to ultraviolet light: (**a**) tensile test specimen, (**b**) disk, (**c**) flexural test specimen after treatment.

2.2. Material Characterization Tests

After completing the parts, tensile and bending tests were conducted following ISO 527-2 (specimen type 1A) [32] and ISO 178 standards [33], using the Shimadzu universal testing machine with a SLBL-5 kN type load cell, at loading rate of 5 mm/min for the tensile test and 3 mm/min for the flexural test, as shown in Figure 3.

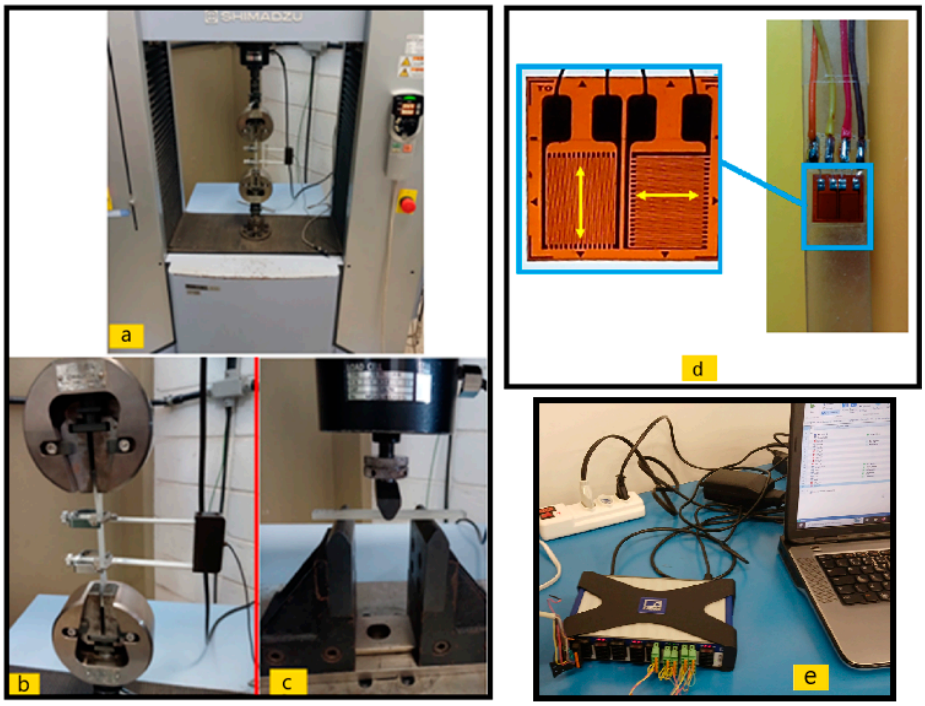

Figure 3. Testing machine used (**a**), setup of specimens for tensile testing (**b**), flexural test setup (**c**), extensometers used (**d**), and DAQ system (**e**).

The purpose of these tests was to determine the Poisson's ratio and the modulus of elasticity (E) of the material for material characterization in finite element simulations. Extensometers were used as shown in Figure 3d, of the BF350-4BB(11) type, with longitudinal and transverse grids, a gage resistance of 349.9 ± 0.2%, and a gage factor of 2.11 ± 1%, together with the HBM Quantum data acquisition system as shown in Figure 3e, to determine the Poisson's ratio. According to the ISO 527 standard [34], 5 specimens were used for each test. The dimensions are listed in Table 2.

Table 2. Dimensions of test specimen used.

Dimensions of the Tensile Test Specimen		Dimensions of the Flexural Test Specimen	
Total length	170 mm	Total length	110 mm
Gauge length (useful length)	80 mm	Width of the cross-section	10 mm
Width of the useful section	10 mm	Height of the cross-section	4 mm
Width of the gripping section	20 mm	Length between beam supports	65 mm
Transition radius	20 mm		
Height of the cross-section	4 mm		

2.3. Photoelasticity and DIC Tests on Disks

For the deformation analysis on the disks, the DIC technique was applied. DIC was conducted using the NCorr software (ncorr v1.2), developed for the MATLAB® environment, as illustrated in Figure 4.

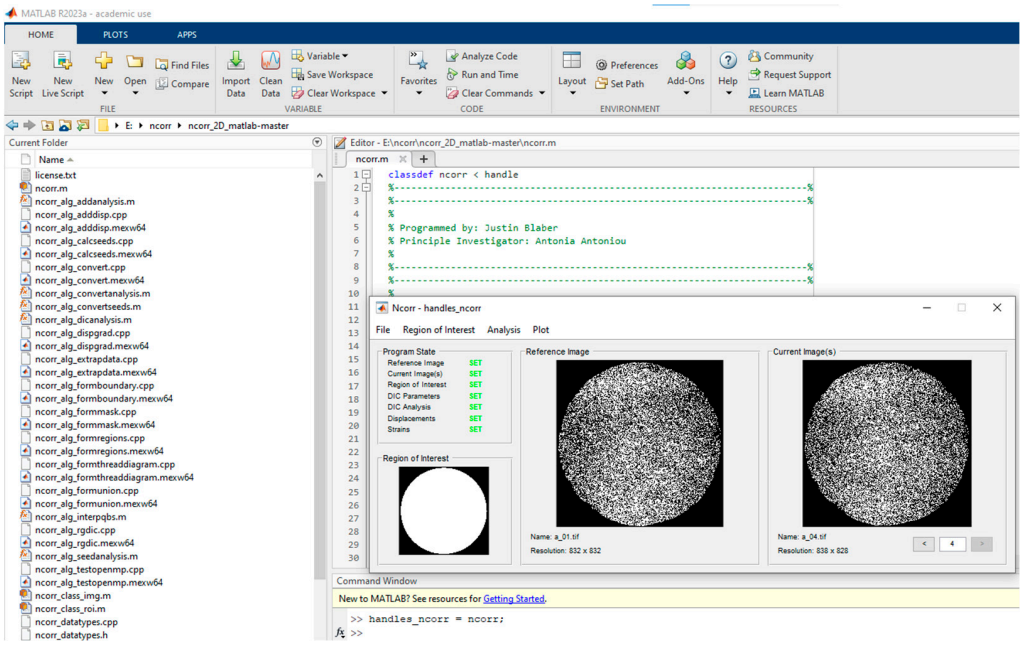

Figure 4. NCorr software interface.

The samples were polished, painted white, and speckled with black paint to create a random pattern that allowed the program code to track point displacements. Video acquisition was performed using a 20 MP smartphone camera mounted on a stand, with a resolution of FHD 1920 × 1080, as shown in Figure 5.

After video acquisition, images/frames of the disks were extracted at load increments (every 1000 N) for use in Ncorr. The images were cropped and processed in batches using ImageJ software (imageJ 154). They were converted to 8-bit gray scale, with color balance adjusted (brightness set to 300), and threshold (default B&W) was applied to enhance and improve point distribution in the image [35–37] as shown in Figure 6.

Figure 7 illustrates the disk before (a) and after processing (b).

The process followed the steps illustrated in Figures 8–10: first, initial parameters for the analysis were defined, including the selection of "seeds" that serve as reference points on the material's surface. Next, the Lagrangian strain model was applied to calculate displacements, enabling the tracking of these points' trajectories [35–37]. Finally, a reference line was drawn to establish the relationship between the actual object length and the number of pixels in the image, allowing for system calibration. This procedure enables the conversion of pixel measurements into real strain values, ensuring the necessary precision

for generating a strain graph that represents the dimensional changes in the material under load [35–37].

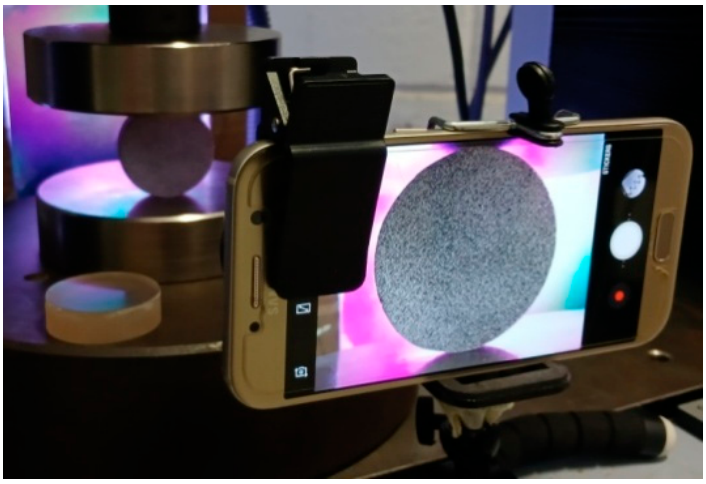

Figure 5. Video acquisition of the DIC test.

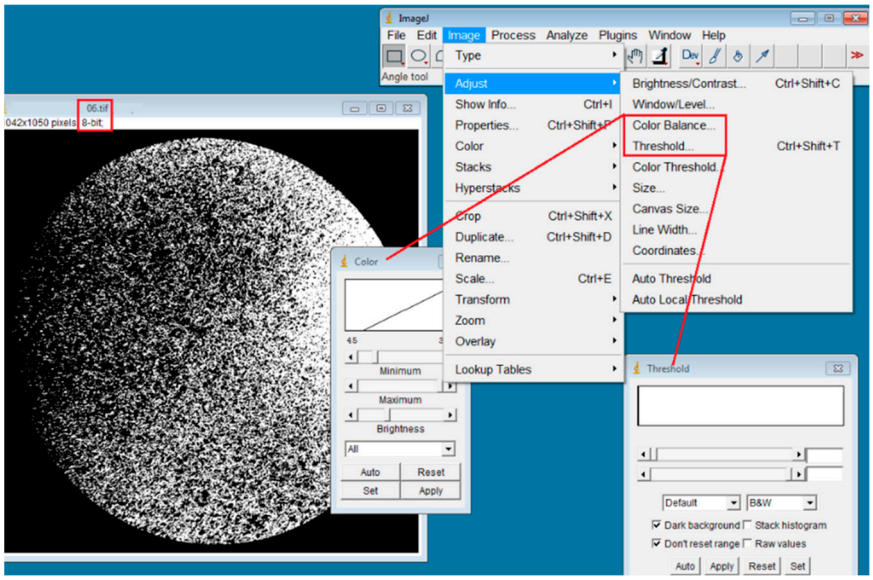

Figure 6. Image processing.

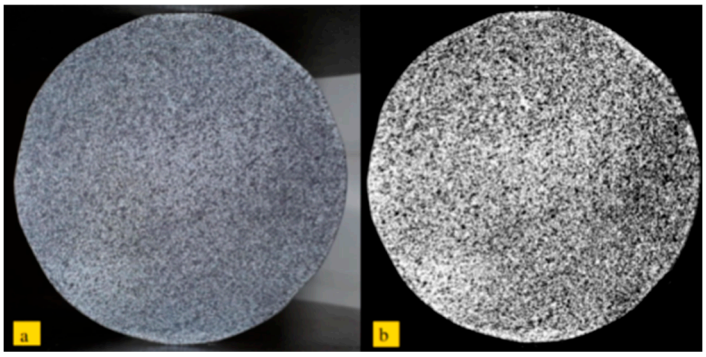

Figure 7. (**a**) Image before processing, (**b**) image after processing.

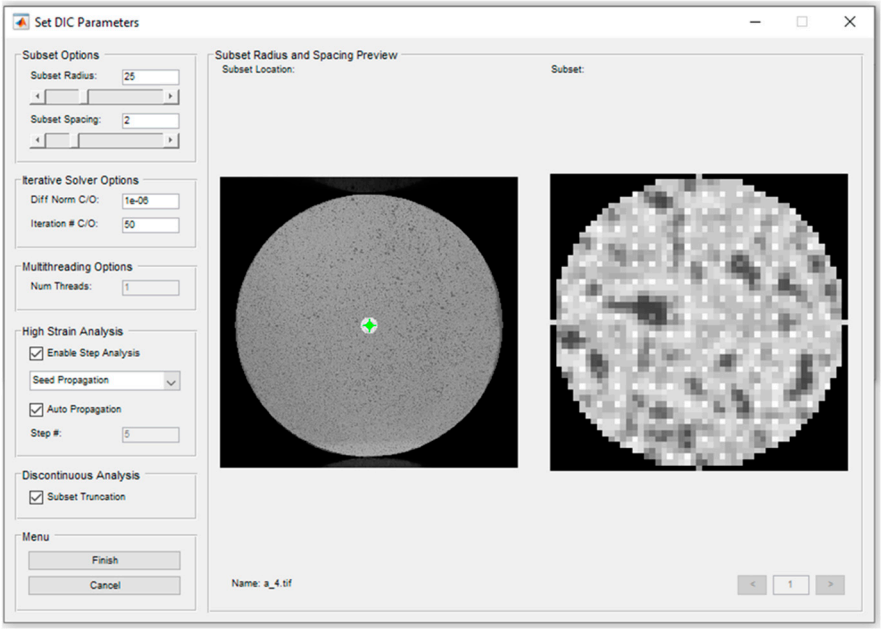

Figure 8. Definition of analysis parameters.

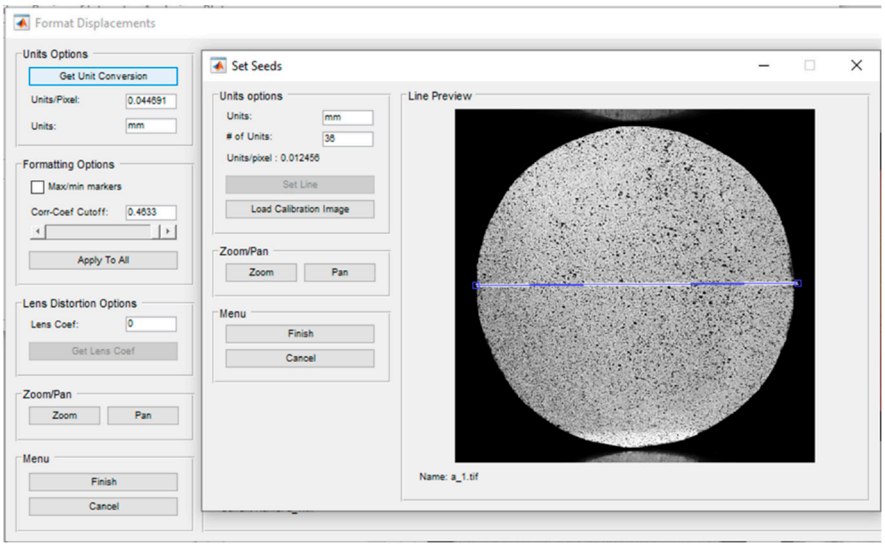

Figure 9. Definition of the relationship between line length and pixels.

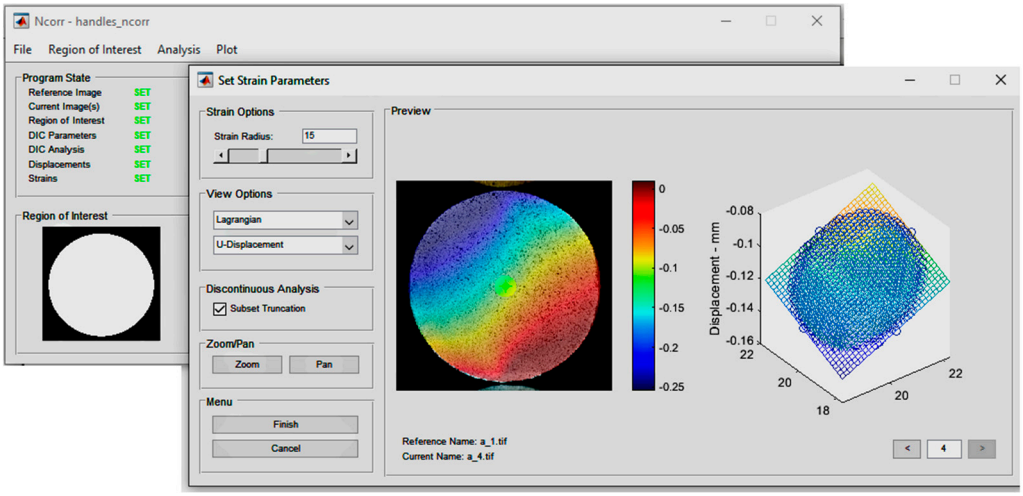

Figure 10. Definition of parameters for strain.

In the study of the stress field behavior of disks under compression, photoelasticity was used. The procedure was implemented with low-cost equipment as shown in Figure 11:

- Two layers of polarizing film (a) placed between the light source and the disk.
- A 35 mm lens with a circular polarizer/linear (CPL) filter (b) attached to the smartphone.

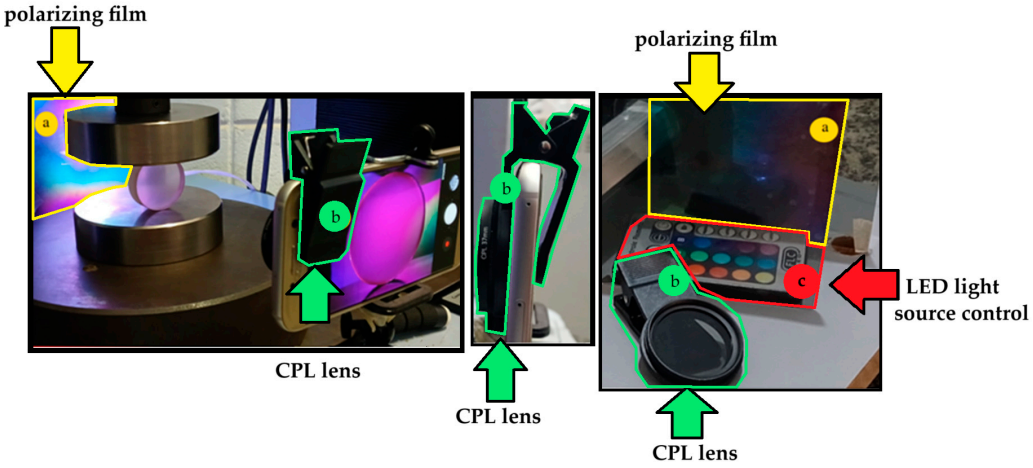

Figure 11. Video acquisition setup for the photoelasticity test and components used: (**a**) polarizing film, (**b**) CPL lens, and (**c**) LED light source control.

The polarizing films were positioned at 90 degrees to each other, and a translucent paper was used to reduce light intensity. The CPL lens was adjusted at 90° relative to the filters as per [23–25]. The light source was an LED lamp with the capability to select color using a remote control, as shown in Figure 11c, facilitating the visualization of photoelastic fringes, which indicate the stress fields in the polished disk [38,39]. After video acquisition, images/frames of the disks were extracted at specific load increments. The compression force applied in the photoelasticity and DIC tests was increased by 20 N per second.

2.4. Numerical and Analytical Methods

The analytical method equations [which define the exact value of the stress field as a function of x and y, with their origin at the center of the disk] were studied according to Equations (1)–(4) from the approaches in [40,41] to accurately predict the stress distribution behavior in the disks during simulations.

$$\begin{Bmatrix} \sigma_x \\ \sigma_y \\ \tau_{xy} \end{Bmatrix} = \frac{-2P}{\pi h} \begin{Bmatrix} \frac{(R-y)x^2}{r_1^4} + \frac{(R+y)x^2}{r_2^4} - \frac{1}{D} \\ \frac{(R-y)^3}{r_1^4} + \frac{(R+y)^3}{r_2^4} - \frac{1}{D} \\ \frac{(R+y)^2 x}{r_2^4} + \frac{(R-y)^2 x}{r_1^4} \end{Bmatrix} \quad (1)$$

- $r_1 = \sqrt{x^2 + (R-y)^2}$;
- $r_2 = \sqrt{x^2 + (R+y)^2}$;
- P: Load [N]
- h: Disk thickness [mm]
- R: Disk radius [mm]
- $D = 2R$;

$$\epsilon_x = \frac{1}{E}(\sigma_x - \nu\sigma_y) \quad (2)$$

$$\epsilon_y = \frac{1}{E}(\sigma_y - \nu\sigma_x) \tag{3}$$

$$\gamma_{xy} = \frac{\tau_{xy}}{E/2(1+\nu)} \tag{4}$$

- ν: Poisson's Ratio.

Two codes were developed to analyze the results of tensile and bending test curves, aiming to identify the point where elastic behavior ends (The Matlab codes are in Appendices A.1 and A.2. Explanations for each code block are provided in lines starting with "%"). This was useful for determining the elastic modulus in both tests and defining the plastic deformation line in the tensile test. Using these data, the material was created in the Ansys library. The tensile test code fits a straight line to the initial points of the data to define the initial linear behavior. Then, it checks each point after this region to identify significant deviations from the calculated straight line. The first point where the deviation exceeds a tolerance limit is marked as the end of linear behavior. The code plots the original data, the initial linear fit line, and marks the point where linearity ends, displaying the displacement and force at this point on the graph. The bending test code processes experimental data from a three-point bending test to convert force and displacement into stress and strain, identify and analyze the linear behavior of the stress–strain curve, calculate the elastic modulus, and plot the results, highlighting the linear region and the point where the behavior transitions from linear to nonlinear.

The equations used the disk dimensions (36 mm diameter and 11 mm thickness), the loading (3000 N, compressive along the y-axis), the resin's modulus of elasticity (1846 MPa), and Poisson's ratio (0.34). The modulus of elasticity used was obtained as the average of the results from the tensile tests (1860 MPa) and the bending tests (1832 MPa). Stress, strain, and shear plots were generated using Matlab software (Matlab r23a).

In performing the numerical simulations, the Static Structural module of the Ansys software was used. Material characterization was achieved by creating a new material in the software library, as shown in Figure 12, based on the experimental data obtained from the mechanical tests (the bulk modulus and shear modulus are automatically populated by the software after specifying the elastic modulus and Poisson's ratio). The test analysis also revealed that the material exhibited a significant plastic deformation region, which was considered in the simulations.

The three-dimensional models of the disks were created in the Design Modeler with the same dimensions as the real ones: a diameter of 36 mm and a thickness of 11 mm. The supports applying compression to the disks were made from structural steel material available in the software library. The contacts between the supports and disks were defined as rough, as shown in Figure 13, to eliminate the need for additional movement constraints; in this case, the coefficient of friction is treated as infinite.

Mesh generation for the simulation was performed using the mesh sizing method, which ensured uniform hexahedral volume. The element size was set to 1 mm. Additionally, the multizone technique was applied to align the element lines at the contact points between supports and disks, as shown in Figure 14. The types of elements used were SOLID186, CONTA174, TARGE170, and SURF154.

This strategy was essential for the Lagrange contact formulation, which enforces non-penetration constraints and contact detection at nodes, as described in [42,43]. The contact algorithm used was the augmented Lagrange method with contact detection at the Gauss integration point, considering the contact stiffness factor equal to 1.0. To define

the boundary conditions for the simulation, the following conditions were established, as shown in Figure 15:

- Compressive Force: applied to the top of the upper support;
- Fixed Support: motion restriction imposed on the bottom face of the lower support.

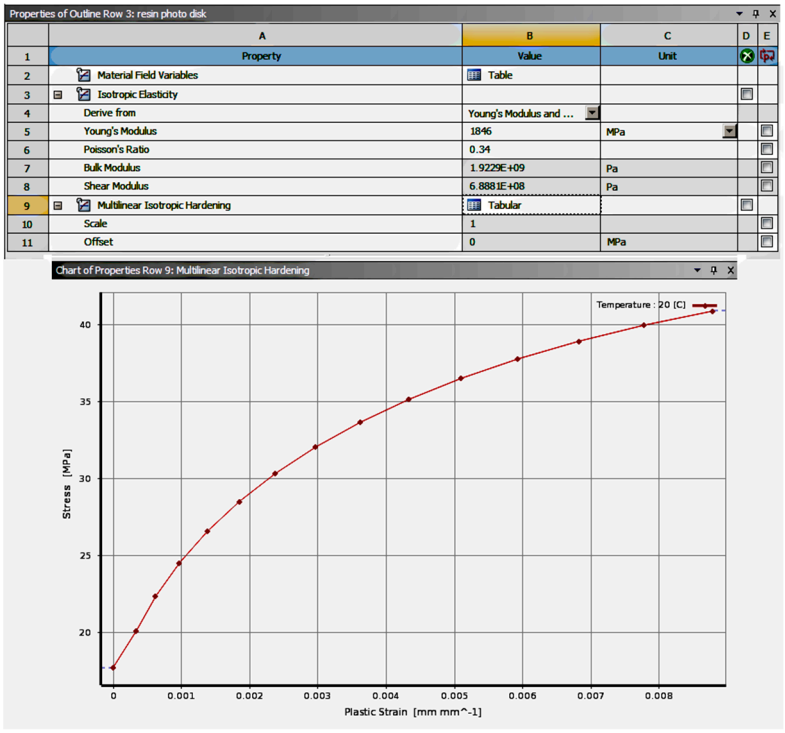

Figure 12. Characterization of the new material in the software.

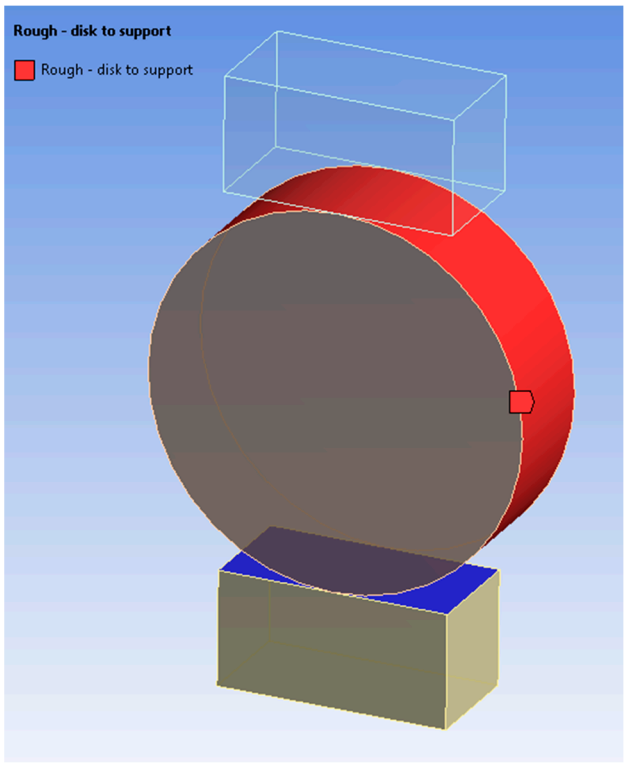

Figure 13. Contact between the supports and the disk.

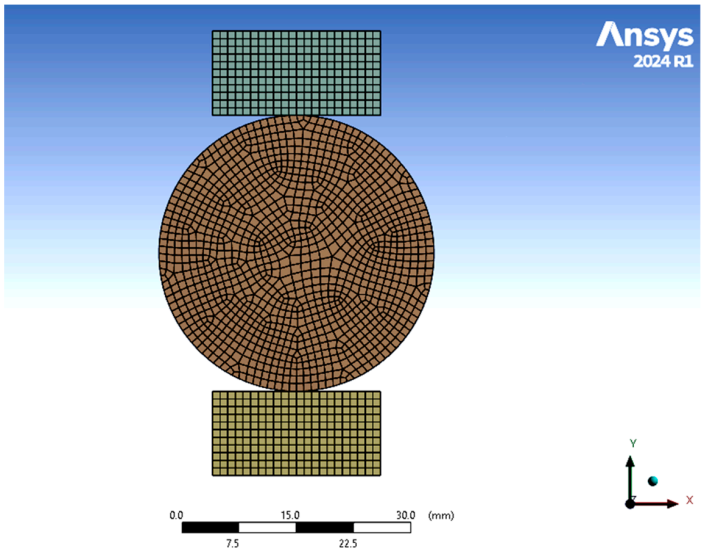

Figure 14. Mesh created on the supports and disk with 82,053 nodes and 18,172 elements.

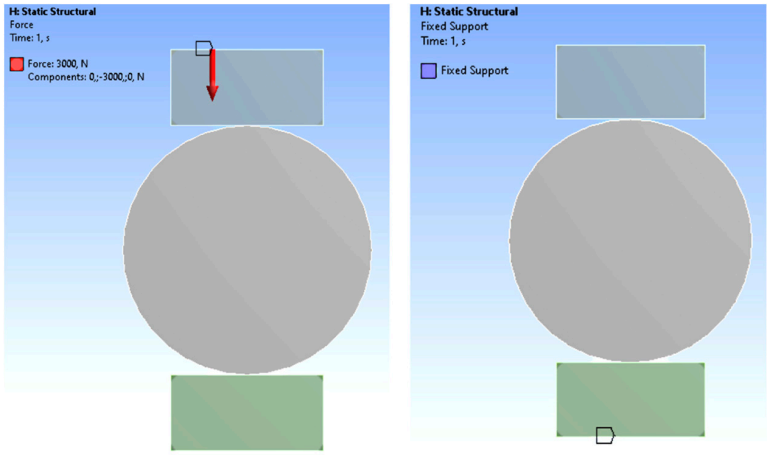

Figure 15. Boundary conditions on the supports and disk.

3. Results

During the photoelasticity test, four color variations of the lamp were examined to determine the most suitable for analysis, as illustrated in Figure 16. The experimental data obtained under an applied load of 3000 N confirmed expectations based on the literature [25–27], which shows a relationship between color variation and the number of fringes. Specifically, white light proved to be the most effective for visualizing fringe variation and chromatic distortion, as illustrated in Figure 16).

A visual representation of the photoelastic behavior in the disk under white light illumination is shown in Figure 17. The loads corresponding to each illustrated frame are detailed in Table 3.

Table 3. Load on each frame, as shown in Figure 17.

Frame	Load
a	0 N
b	50 N
c	150 N
d	300 N
e	600 N
f	1300 N
g	1700 N
h	3000 N

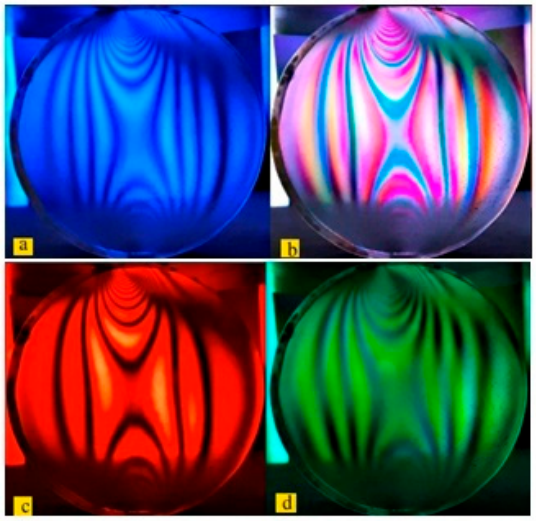

Figure 16. Fringe distribution as a function of the light source color: (**a**) blue, (**b**) white, (**c**) red, (**d**) green.

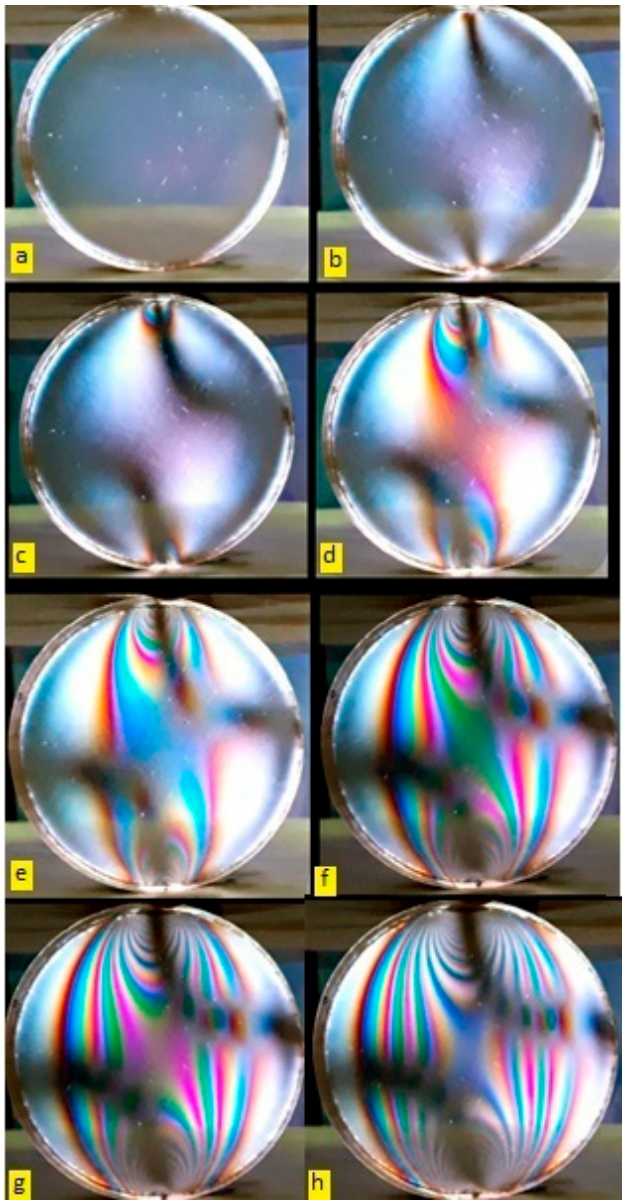

Figure 17. Loading in each frame.

The normal stress fields in the x and y directions, obtained by the analytical method, are graphically represented in Figures 18 and 19. Additionally, the shear stress in the xy plane is illustrated in Figure 20. The applied load was 3000 N in all three figures.

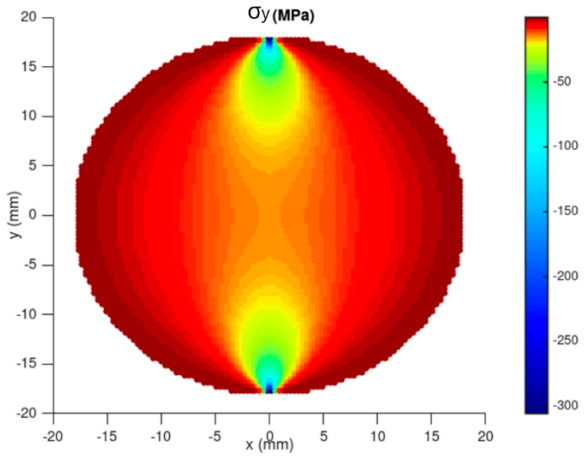

Figure 18. Normal stress in the y direction.

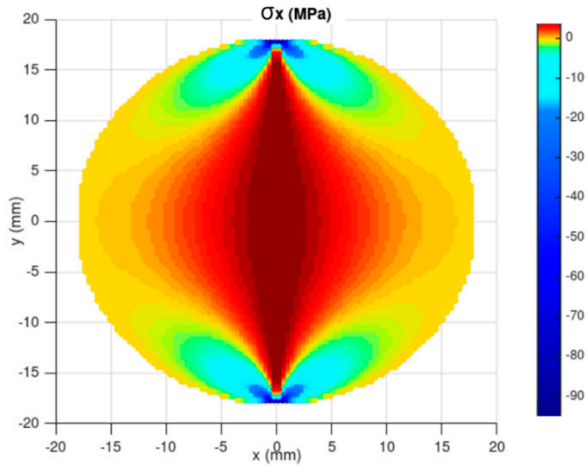

Figure 19. Normal stress in the x direction.

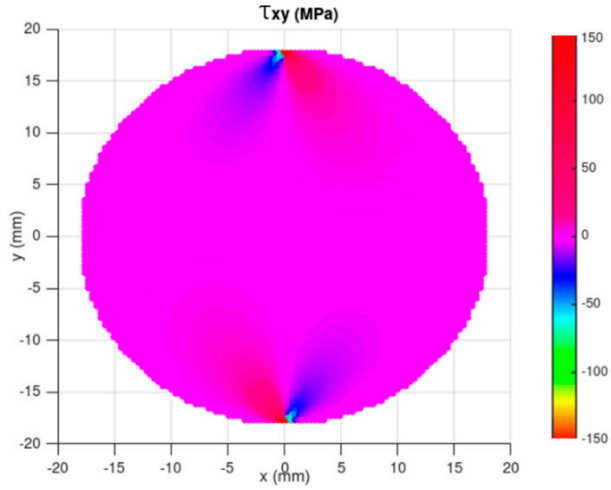

Figure 20. Shear stress in the xy plane.

In Figure 21, the correlation between the studied methods and the image recorded during the photoelasticity test was observed in the normal stress distribution profile in

the y-direction. After adjusting the colors of the graph to improve visualization and simulation, it was found that the models accurately replicated the fringe behavior observed experimentally. With the normal stress results converging, comparisons of specific strains between the methods could be made.

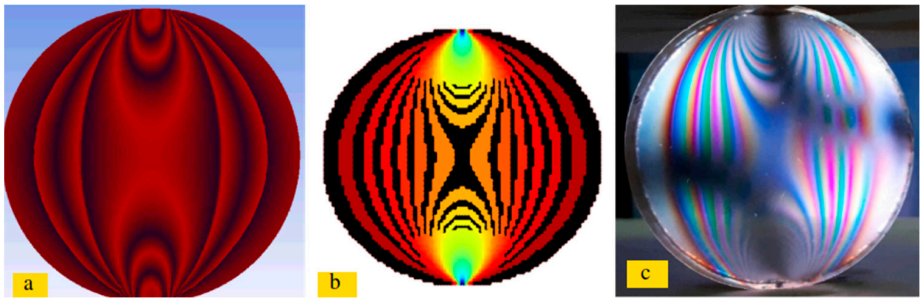

Figure 21. Fringe patterns according to the methods: (**a**) numerical, (**b**) analytical, and (**c**) photoelasticity.

The comparison of specific strain in the x, y directions, and in the xy plane between the methods is illustrated in Figures 22–24. The probe feature was used to identify strain values in similar regions across each method. The specific strain field, illustrated in Figures 18–20, shows similar behavior to the stress field, manifesting as concentric circular patterns near the contact area.

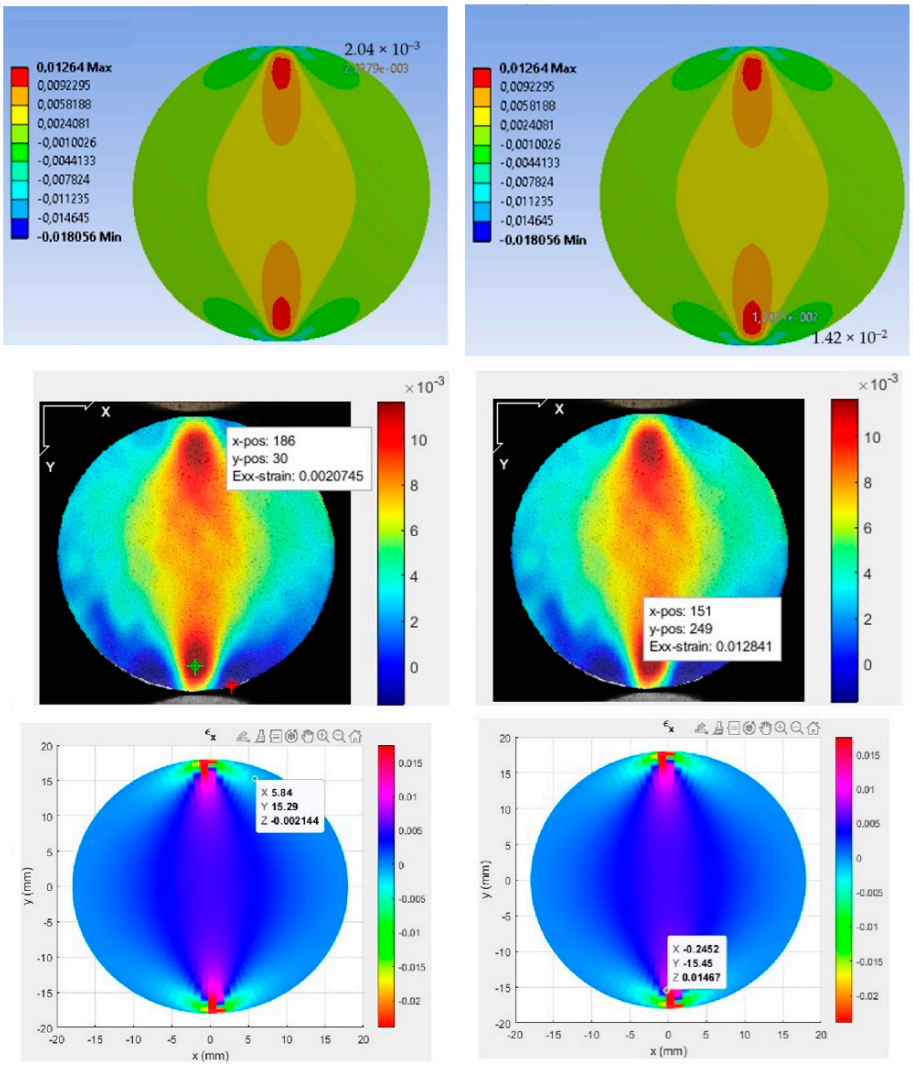

Figure 22. Specific strain in the y-direction in the simulation, DIC, and analytical methods.

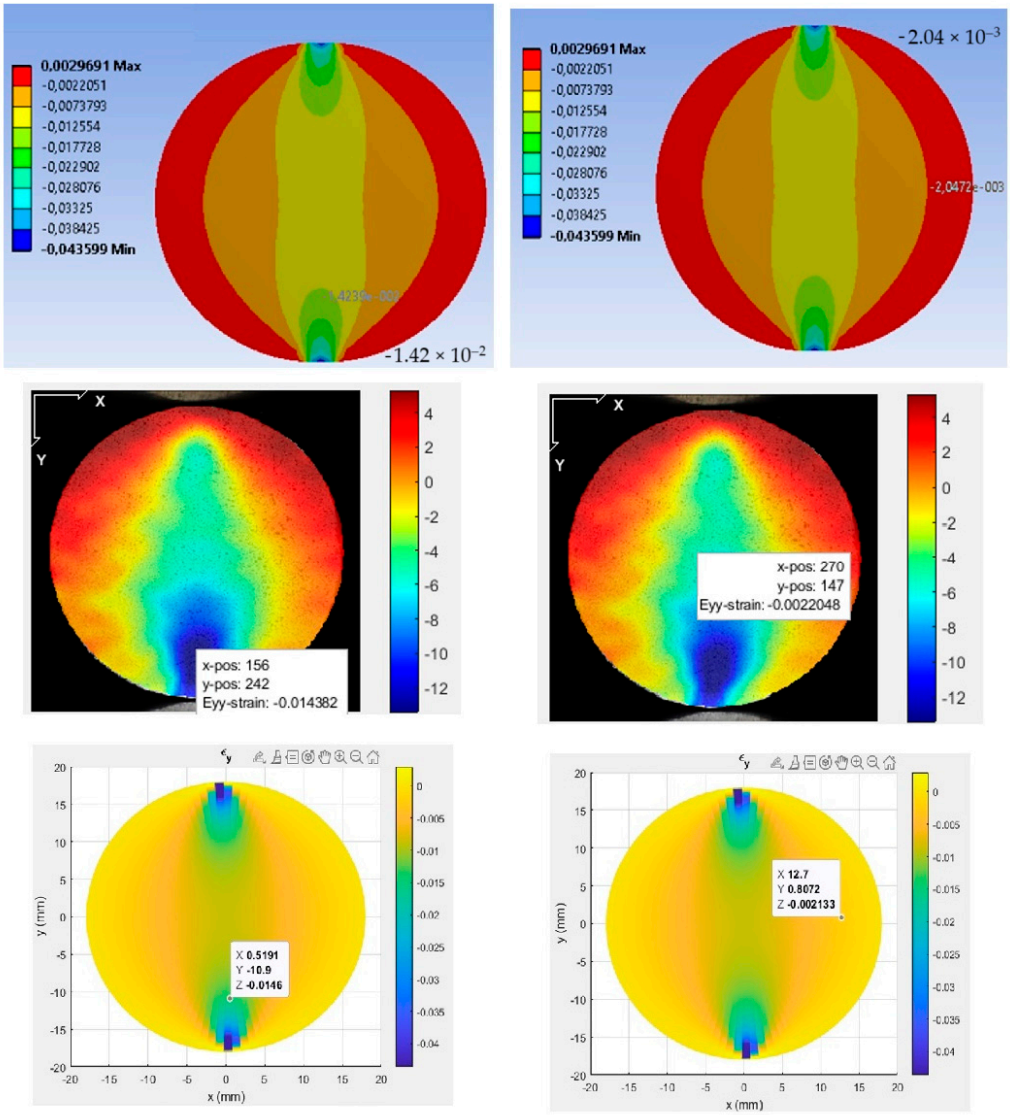

Figure 23. Specific strain in the x-direction in the simulation, DIC, and analytical methods.

Tables 4 and 5 detail the strain values obtained and the comparative percentage error according to Equation (5) between the methods considering the load of 3000 N.

$$error = \left(\frac{A - B}{A}\right) \times 100 \tag{5}$$

Table 4. Strain modulus value (mm/mm).

Numerical	DIC	Analytical
	x-Direction	
1.42×10^{-2} 2.04×10^{-3}	1.43×10^{-2} 2.20×10^{-3}	1.46×10^{-2} 2.14×10^{-3}
	y-Direction	
2.04×10^{-3} 1.42×10^{-2}	2.20×10^{-3} 1.43×10^{-2}	2.22×10^{-3} 1.40×10^{-2}
	xy-Plane	
5.55×10^{-5} 5.51×10^{-4}	5.75×10^{-5} 5.96×10^{-4}	5.60×10^{-5} 5.79×10^{-4}

Table 5. Comparative percentage error between methods.

Numerical/DIC	Numerical/Analytical	DIC/Analytical
	x-Direction	
1.00% 7.69%	3.02% 4.72%	2.00% 2.75%
	y-Direction	
7.69% 0.62%	8.8316% 1.4678%	1.05% 2.07%
	xy-Plane	
3.57% 8.25%	0.82% 5.19%	2.65% 2.81%

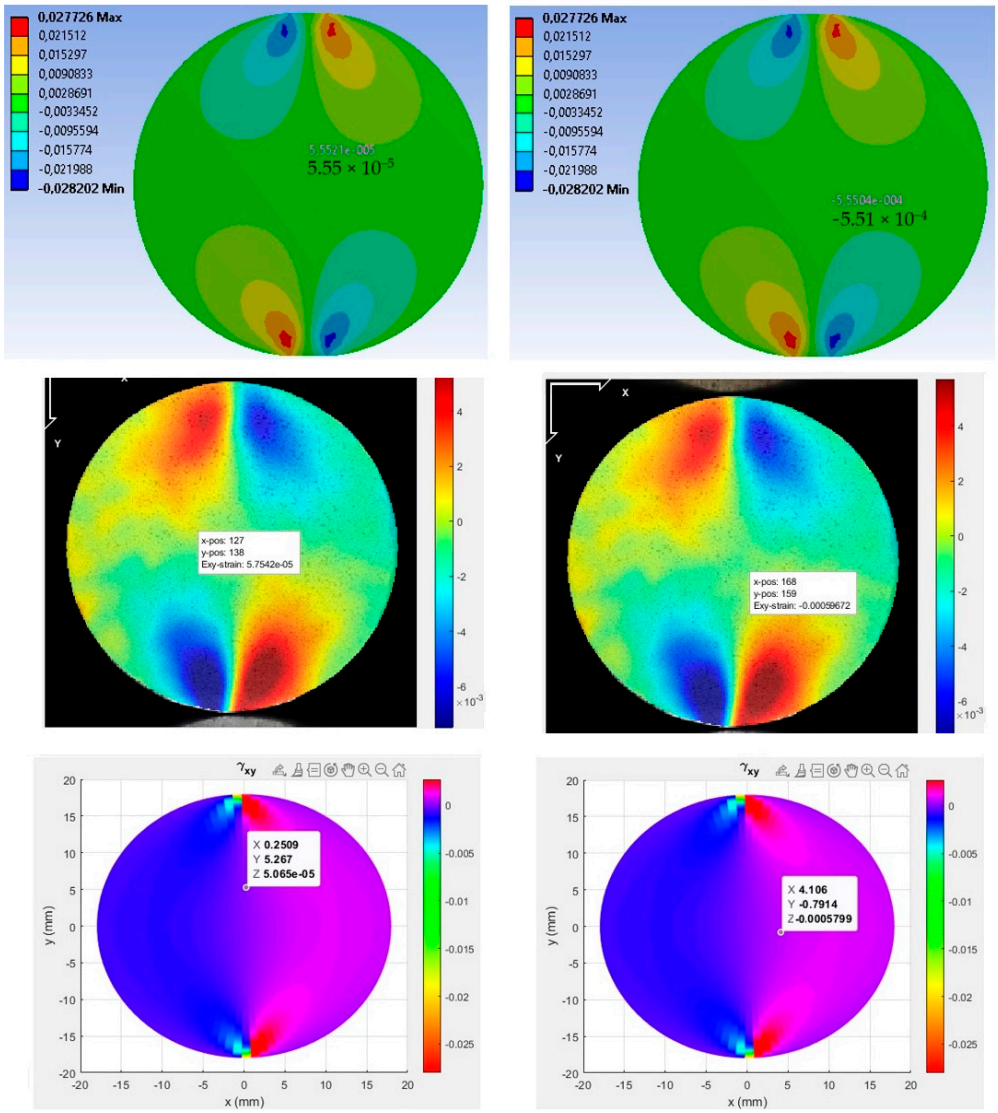

Figure 24. Specific strain in the xy plane in the simulation, DIC, and analytical methods.

4. Discussion

The analysis of the results indicates that, although DIC shows good compatibility with numerical and analytical methods in the x direction, it presented more pronounced limitations in the y and xy directions in this study. Compared to the numerical method, DIC shows a percentage error of 1.00% in the x-direction, indicating a reasonable match; however, in the y and xy directions, the errors increase significantly, reaching 7.69% and

8.25%, respectively, suggesting lower accuracy of DIC in capturing the deformations observed by the numerical method in these directions. Similarly, compared to the analytical method, DIC maintains a relatively low error in the x-direction (2.00%) but shows greater variation in the y and xy directions, with errors of 1.05% and 2.65%.

These findings align with studies such as Maedeh et al. [18], which demonstrate the effectiveness of DIC in characterizing material properties despite some discrepancies in specific scenarios. The observed limitations in the y and xy directions highlight the need for careful consideration when applying DIC in studies requiring high accuracy in complex strain patterns. However, advancements in the integration of low-cost tools, as noted by Arabul and Lunt [14], and the use of open-source software, such as Ncorr, provide avenues to enhance the accessibility and economic feasibility of DIC, making it a viable option despite its limitations.

Furthermore, the use of photoelasticity, as described by Curtis et al. [11] and Ren and Ju [13], offers a complementary approach to visualizing stress fields in real-time. While DIC excels in capturing detailed strain data, photoelasticity leverages optical properties to provide qualitative insights into stress distributions. The combination of these techniques can help address the limitations observed in DIC, especially in the y and xy directions, providing a broader perspective on material behavior.

Recent advancements in the properties of photosensitive resins and 3D printing, as discussed by Wang et al. [10] and Ren and Ju [13], also suggest potential improvements for experimental setups. Enhanced materials and printing techniques can mitigate issues, such as anisotropy and residual birefringence, thereby improving the accuracy and reliability of both DIC and photoelasticity in experimental studies.

These differences, although moderate, indicate that DIC may have limitations in accurately representing deformations in the y and xy directions, especially in areas with varied strain patterns in this study of compression disks. However, when combined with complementary techniques, such as photoelasticity, and supported by numerical simulations and analytical methods, these approaches collectively provide a comprehensive framework for the study of stress and strain fields.

5. Conclusions

The procedures carried out in this study, using low-cost equipment, demonstrated feasibility in the analysis of stress and strain in translucent polymers. Each method employed presented its particularities and adjustment requirements. Photoelasticity depends on factors such as disk polishing, light source parameters (color, intensity), and the angle at which the CPL lens was adjusted relative to the filters. The DIC method requires specific software parameters (pre-treatment of video frames, selection of the study region, mathematical model used), a homogeneous point distribution in the paint, and adequate sharpness in the generated frames. The numerical method depends on the defined boundary conditions, the type of contact, the selected mathematical model (Lagrange, penalty, etc.), and material characterization.

The results demonstrate that, with the parameters described in the literature, these methods are effective and accurate for experimental studies in educational environments and prototype development, confirming their validity and reliability as an alternative approach.

In addition to contributing to technical and professional education by facilitating the visual understanding of stress and strain fields, the methodology proved promising for additive manufacturing processes with resin, validating simulations and practical experiments. In the future, its application to studies on contact stresses in gears is planned, where it is expected to further enhance its relevance and practical applicability, solidifying it as an accessible and reliable approach in scientific and educational contexts.

Author Contributions: Conceptualization, methodology, validation, G.C.R.d.O.; writing—review and editing, V.A.R.d.O. and C.A.A.S.; supervision, E.S.G. and F.d.A.S. All authors have read and agreed to the published version of the manuscript.

Funding: This work was supported in part by "Coordenação de Aperfeiçoamento de Pessoal de Nível Superior—Brasil (CAPES)—Finance Code 001".

Data Availability Statement: The original contributions presented in this study are included in the article. Further inquiries can be directed to the corresponding author(s).

Conflicts of Interest: The authors declare no conflicts of interest.

Appendix A

Appendix A.1. Matlab Code for Analysis of Linear Behavior in Tensile Test

The code fits a straight line to the initial points of the data to define the initial linear behavior in tensile test. Then, it checks each point after this initial region to identify significant deviations from the calculated straight line. The first point where the deviation exceeds a tolerance limit is marked as the end of linear behavior. The code plots the original data, the initial linear fit line, and marks the point where linearity ends, displaying the displacement and force at this point on the graph.

```
% Displacement (x) and force (y) data already provided as vectors
% Example: x = [displacement values]; y = [force values];

% Parameters for analysis
initial_window_size = 150; % Number of initial points to define the linear region
error_limit = 0.01 * max(y); % Error limit to identify the end of linearity

% Linear fit to the first points to define the initial linear behavior
p = polyfit(x(1:initial_window_size), y(1:initial_window_size), 1);
initial_linear_fit = polyval(p, x);

% Find the point where the deviation from the initial linear behavior exceeds the limit
linear_end_index = NaN; % Initialize the index for the end of linear behavior
for i = initial_window_size + 1: length(x)
% Calculate the deviation from the initial linear fit
deviation = abs(y(i)—initial_linear_fit(i));

% Check if the deviation exceeds the error limit
if deviation > error_limit
linear_end_index = i;
break;
end
end

% Plot the data
figure;
plot(x, y, 'b-', 'DisplayName', 'Original Data');
hold on;

if ~isnan(linear_end_index)
% Show the linear region fitted up to the end of linearity point
plot(x(1:linear_end_index), initial_linear_fit(1:linear_end_index), 'r--', 'DisplayName', 'Linear Behavior');
plot(x(linear_end_index), y(linear_end_index), 'go', 'MarkerSize', 10, 'DisplayName', 'End of Linear Behavior');
```

```
disp(['Linear behavior ends at: Displacement = ', num2str(x(linear_end_index)), ...
'mm, Force = ', num2str(y(linear_end_index)), 'N']);
else
disp('Could not find the end point of linear behavior.');
end

xlabel('Displacement (mm)');
ylabel('Force (N)');
legend;
title('Analysis of Linear Behavior in Tensile Test');
grid on;
```

Appendix A.2. Matlab Code for Analysis of Bending Elastic Modulus

The code processes experimental data from a three-point bending test to: Convert force and displacement into stress and strain. Identify and analyze the linear behavior of the stress–strain curve. Calculate the elastic modulus. Plot the results, highlighting the linear region and the point where the behavior transitions from linear to nonlinear.

```
% Deformation (x) and force (y) data already provided as vectors
% Example: x = [deformation values]; y = [force values];

% Parameters for analysis
initial_window_size = 3200; % Number of initial points to define the linear region
error_limit = 0.0001 * max(y); % Error limit to identify the end of linearity

% Three-point bending test data
L = 64.7; % Length between beam supports (mm)
L_0 = 110; % Total length of the beam (mm)
b = 9.93; % Width of the cross-section (mm)
h = 4.41; % Height of the cross-section (mm)

% Calculating the moment of inertia of the cross-section (I) for a rectangular section
I = (b * h^3)/12; % Moment of inertia (mm^4)

% Converting force data (y) to stress (σ = M/S), with M = F * L/4
stress = (1.5 * y * L)/(b * h^2); % Bending stress in MPa

% Converting displacement data (x) to strain (ε = (6 * x * h)/(L^2))
specific_strain = (6 * x * h)/(L^2); % Specific strain (unitless)

% Linear fit on the initial points to define the initial linear behavior
p = polyfit(specific_strain(1:initial_window_size), stress(1:initial_window_size), 1);
initial_linear_fit = polyval(p, specific_strain(1:initial_window_size)); % Linear fit for initial points
only

% Finding the point where the deviation from initial linear behavior exceeds the limit
end_linear_index = NaN; % Initialize the end of linear behavior index
for i = initial_window_size + 1: length(specific_strain)
% Calculate the deviation from the initial linear fit
deviation = abs(stress(i)—polyval(p, specific_strain(i))); % Compare with the fitted value at
specific_strain(i)
```

```
% Check if the deviation exceeds the error limit
if deviation > error_limit
end_linear_index = i;
break;
end
end

% Plot the data
figure;
plot(specific_strain, stress, 'b-', 'DisplayName', 'Original Data');
hold on;

if ~isnan(end_linear_index)
% Fit a linear line for the points up to the end of linearity
partial_linear_fit = polyval(p, specific_strain(1:end_linear_index)); % Linear fit up to the end of
linearity

% Display the linear region fit up to the end of linearity
plot(specific_strain(1:end_linear_index), partial_linear_fit, 'r--', 'DisplayName', 'Linear Behavior');
plot(specific_strain(end_linear_index), stress(end_linear_index), 'go', 'MarkerSize', 10,
'DisplayName', 'End of Linear Behavior');
disp(['The linear behavior ends at: Strain = ', num2str(specific_strain(end_linear_index)), ...
', Stress = ', num2str(stress(end_linear_index)), 'MPa']);

% Calculate and display the Elastic Modulus (slope of the linear fit)
elastic_modulus = p(1); % Slope of the linear fit
disp(['The Elastic Modulus is: ', num2str(elastic_modulus), 'MPa']);
else
disp('Could not find the end point of linear behavior.');
end

xlabel('Specific Strain (mm/mm)');
ylabel('Stress (MPa)');
legend;
title('Linear Behavior Analysis in Three-Point Bending Test');
grid on;
```

References

1. Berthelot, J.M. *Composite Materials: Mechanical Behavior and Structural Analysis*, 1st ed.; Springer Science & Business Media: New York, NY, USA, 2012.
2. Krzywanski, J.; Sosnowski, M.; Grabowska, K.; Zylka, A.; Lasek, L.; Kijo-Kleczkowska, A. Advanced Computational Methods for Modeling, Prediction and Optimization—A Review. *Materials* **2024**, *17*, 3521. [CrossRef] [PubMed]
3. Vergara, D.; Extremera, J.; Rubio, M.P.; Dávila, L.P. Meaningful Learning Through Virtual Reality Learning Environments: A Case Study in Materials Engineering. *Appl. Sci.* **2019**, *9*, 4625. [CrossRef]
4. Bernard, C.A.; Correia JP, M.; Ahzi, S.; Bahlouli, N. Numerical implementation of an elastic-viscoplastic constitutive model to simulate the mechanical behaviour of amorphous polymers. *Int. J. Mater. Form.* **2017**, *10*, 607–621. [CrossRef]
5. Varna, J.; Pupure, L. Effect of Material State and Temperature on Nonlinear Viscoelastic Response: 3D Constitutive Model and Incremental Formulation for Numerical Analysis. *Mech. Compos. Mater.* **2023**, *59*, 193–218. [CrossRef]
6. Abu Al-Rub, R.K.; Tehrani, A.H.; Darabi, M.K. Application of a large deformation nonlinear-viscoelastic viscoplastic viscodamage constitutive model to polymers and their composites. *Int. J. Damage Mech.* **2015**, *24*, 198–244. [CrossRef]
7. Yin, B.; Kaliske, M. Fracture simulation of viscoelastic polymers by the phase-field method. *Comput. Mech.* **2020**, *65*, 293–309. [CrossRef]
8. Kamenskikh, A.A.; Nosov, Y.O.; Bogdanova, A.P. The Study Influence Analysis of the Mathematical Model Choice for Describing Polymer Behavior. *Polymers* **2023**, *15*, 3630. [CrossRef] [PubMed]

9. Gdoutos, E.E. Photoelasticity. In *Experimental Mechanics. Solid Mechanics and Its Applications*; Springer: Cham, Switzerland, 2022; Volume 269. [CrossRef]
10. Wang, L.; Ju, Y.; Xie, H.; Ma, G.; Mao, L.; He, K. The mechanical and photoelastic properties of 3D printable stress-visualized materials. *Sci. Rep.* **2017**, *7*, 10918. [CrossRef] [PubMed]
11. Curtis, J.D.; Hanna, S.D.; Patterson, E.A.; Taroni, M. On the use of stereolithography for the manufacture of photoelastic models. *Exp. Mech.* **2003**, *43*, 148–162. [CrossRef]
12. Ramesh, K.; Sasikumar, S. Digital photoelasticity: Recent developments and diverse applications. *Opt. Lasers Eng.* **2020**, *135*, 106186. [CrossRef]
13. Ren, Z.; Ju, Y. Optical anisotropy of transparent polymer materials fabricated via 3D printing and their application in photoelasticity. *Opt. Mater.* **2023**, *138*, 113743. [CrossRef]
14. Arabul, E.; Lunt, A.J.G. A Novel Low-Cost DIC-Based Residual Stress Measurement Device. *Appl. Sci.* **2022**, *12*, 7233. [CrossRef]
15. Ab Ghani, A.F.; Mahmud, J.; Nazran, S.; Muhammad, N. Mechanical properties extraction of composite material using digital image correlation via open source Ncorr. *Def. S T Tech. Bull.* **2018**, *11*, 13–24.
16. Kumar, S.L.; Aravind, H.B.; Hossiney, N. Digital image correlation (DIC) for measuring strain in brick masonry specimen using Ncorr open source 2D MATLAB program. *Results Eng.* **2019**, *4*, 100061. [CrossRef]
17. Quanjin, M.; Rejab, M.R.M.; Halim, Q.; Merzuki, M.N.M.; Darus, M.A.H. Experimental investigation of the tensile test using digital image correlation (DIC) method. *Mater. Today Proc.* **2020**, *27*, 757–763. [CrossRef]
18. Amirpour, M.; Bickerton, S.; Calius, E.; Das, R.; Mace, B. Numerical and experimental study on deformation of 3D-printed polymeric functionally graded plates: 3D-Digital Image Correlation approach. *Compos. Struct.* **2019**, *211*, 481–489. [CrossRef]
19. Li, W.; Nee, A.Y.C.; Ong, S.K. A State-of-the-Art Review of Augmented Reality in Engineering Analysis and Simulation. *Multimodal Technol. Interact.* **2017**, *1*, 17. [CrossRef]
20. Zhu, K.; Cao, J.; Chen, G.; He, Q.; Zhang, P. A General Construction Method of Virtual Simulation Experiment Platform Based on Bibliometrics and Analytic Hierarchy Process. *Educ. Sci.* **2023**, *13*, 80. [CrossRef]
21. Camargo, C.; Gonçalves, J.; Conde, M.Á.; Rodríguez-Sedano, F.J.; Costa, P.; García-Peñalvo, F.J. Systematic Literature Review of Realistic Simulators Applied in Educational Robotics Context. *Sensors* **2021**, *21*, 4031. [CrossRef]
22. Chatpinyakoop, C.; Hallinger, P.; Showanasai, P. Developing Capacities to Lead Change for Sustainability: A Quasi-Experimental Study of Simulation-Based Learning. *Sustainability* **2022**, *14*, 10563. [CrossRef]
23. Atkinson, D.; Becker, T. A 117 Line 2D Digital Image Correlation Code Written in MATLAB. *Remote Sens.* **2020**, *12*, 2906. [CrossRef]
24. Statnik, E.S.; Dragu, C.; Besnard, C.; Lunt, A.J.G.; Salimon, A.I.; Maksimkin, A.; Korsunsky, A.M. Multi-Scale Digital Image Correlation Analysis of In Situ Deformation of Open-Cell Porous Ultra-High Molecular Weight Polyethylene Foam. *Polymers* **2020**, *12*, 2607. [CrossRef]
25. Belloni, V.; Ravanelli, R.; Nascetti, A.; Di Rita, M.; Mattei, D.; Crespi, M. py2DIC: A New Free and Open Source Software for Displacement and Strain Measurements in the Field of Experimental Mechanics. *Sensors* **2019**, *19*, 3832. [CrossRef] [PubMed]
26. Vargas-Isaza, C.; Posada-Correa, J.; Briñez-de León, J. Analysis of the Stress Field in Photoelasticity Used to Evaluate the Residual Stresses of a Plastic Injection-Molded Part. *Polymers* **2023**, *15*, 3377. [CrossRef]
27. Kim, S.; Nam, B.-H.; Jung, Y.-H. Evaluating Variability in Reflective Photoelasticity: Focus on Adhesives, Light Sources, and Camera Setup. *Appl. Sci.* **2023**, *13*, 10628. [CrossRef]
28. Marín-Miranda, M.; Wintergerst, A.M.; Moreno-Vargas, Y.A.; Juárez-López, M.L.A.; Tavera-Ruiz, C. Photoelasticity for Stress Concentration Analysis in Dentistry and Medicine. *Materials* **2022**, *15*, 6819. [CrossRef]
29. Vieira, F.G.; Scari, A.S.; Magalhães Júnior, P.A.A.; Martins, J.S.R.; Magalhães, C.A. Analysis of Stresses in a Tapered Roller Bearing Using Three-Dimensional Photoelasticity and Stereolithography. *Materials* **2019**, *12*, 3427. [CrossRef]
30. Herráez-Galindo, C.; Torres-Lagares, D.; Martínez-González, Á.-J.; Pérez-Velasco, A.; Torres-Carranza, E.; Serrera-Figallo, M.-A.; Gutiérrez-Pérez, J.-L. A Comparison of Photoelastic and Finite Elements Analysis in Internal Connection and Bone Level Dental Implants. *Metals* **2020**, *10*, 648. [CrossRef]
31. Cuan-Urquizo, E.; Barocio, E.; Tejada-Ortigoza, V.; Pipes, R.B.; Rodriguez, C.A.; Roman-Flores, A. Characterization of the Mechanical Properties of FFF Structures and Materials: A Review on the Experimental, Computational and Theoretical Approaches. *Materials* **2019**, *12*, 895. [CrossRef]
32. *ISO 527-2*; Plastics—Determination of Tensile Properties—Part 2: Test Conditions for Moulding and Extrusion Plastics. ISO: Geneva, Switzerland, 2012.
33. *ISO 178*; Plastics—Determination of Flexural Properties. ISO: Geneva, Switzerland, 2019.
34. *ISO 527*; Plastics—Determination of Tensile Properties—Part 1: General Principles. ISO: Geneva, Switzerland, 2019.
35. Blaber, J.; Adair, B.; Antoniou, A. Ncorr: Open-Source 2D Digital Image Correlation Matlab Software. *Exp. Mech.* **2015**, *55*, 1105–1122. [CrossRef]
36. Irwansyah, I.; Dirhamsyah, M.; Iswardy, E.; Aulia, T.N.; Alkindi, M.; Fitriani, S.D. Experimental Study of Strain Measurement using 2D Digital Image Correlation on Fixation Plate and Calcaneus Bone Fracture. *J. Phys. Conf. Ser.* **2024**, *2739*, 12049. [CrossRef]

37. Tambusay, A.; Suryanto, B.; Suprobo, P. Digital image correlation for cement-based materials and structural concrete testing. *Civ. Eng. Dimens.* **2020**, *22*, 6–12. [CrossRef]
38. Muthu, S.; Schuurmans, F.J.; Pashley, M.D. Red, green, and blue LED based white light generation: Issues and control. In Proceedings of the Conference Record of the 2002 IEEE Industry Applications Conference, 37th IAS Annual Meeting (Cat. No. 02CH37344), Pittsburgh, PA, USA,, 13–18 October 2002; IEEE: Piscataway, NJ, USA, 2002; Volume 1, pp. 327–333.
39. Uchida, Y.; Taguchi, T. Lighting theory and luminous characteristics of white light-emitting diodes. *Opt. Eng.* **2005**, *44*, 124003. [CrossRef]
40. Ramesh, K. *Developments in Photoelasticity*; IOP Publishing: Bristol, UK, 2021; pp. 2053–2563.
41. Magalhaes, C.A.; Neto, P.S.; Magalhaes, P.A.A.; de Barcellos, C.S. Numerical Methods for the Photoelastic Technique using Phase Shifting. *J. Mech.* **2015**, *31*, 355–367. [CrossRef]
42. Doca, T.; Pires, F.A. Analysis of a cylinder-to-flat contact problem at finite elasto-plastic strains. *Tribol. Int.* **2014**, *79*, 92–98. [CrossRef]
43. Bonhin, E.P.; Müzel, S.D.; de Oliveira, G.C.R.; Medeiros Tupinambá, W.L.; Guidi, E.S.; Alvarado Silva, C.A.; de Azevedo Silva, F. Evaluation and Feasibility of Different Models and Methods for Composite Simulation Using Ansys. *IAENG Int. J. Comput. Sci.* **2024**, *51*, 918–924.